Realization of Repulsive Polarons in the Strongly Correlated Regime

R. Henke[1], J. Levinsen[2], M. M. Parish[2], J. Boronat[3], G. E. Astrakharchik[3], H. Moritz[1,4,*] and C. R. Cabrera[1,4,5,†]

[1]*Institute for Quantum Physics, Universität Hamburg, Luruper Chaussee 149, 22761 Hamburg, Germany*
[2]*School of Physics and Astronomy, Monash University, Victoria 3800, Australia*
[3]*Departament de Física, Campus Nord B4-B5, Universitat Politècnica de Catalunya, E-08034 Barcelona, Spain*
[4]*The Hamburg Centre for Ultrafast Imaging, Universität Hamburg, Luruper Chaussee 149, 22761 Hamburg, Germany*
[5]*Instituto Galego de Física de Altas Enerxías, Universidade de Santiago de Compostela, Santiago de Compostela 15782, Spain*

(Received 11 December 2025; accepted 24 August 2026; published 13 November 2026)

Mobile impurities interacting with a quantum medium form quasiparticles known as polarons, a central concept in many-body physics. While the quantum impurity problem has been extensively studied with ultracold atomic gases, repulsive polarons in the strongly correlated regime have remained elusive. Typically, the impurity atoms bind into molecules or rapidly decay into deeper-lying states before they can acquire an appreciable dressing cloud. Here, we report on the realization of polarons in a strongly repulsive two-dimensional quantum gas. Using a superfluid of ^{6}Li dimers, we introduce impurities by promoting a small fraction of the dimers into higher levels of the transverse confining potential. These novel synthetic-spin polarons give access to the strongly repulsive regime where common decay channels are suppressed. We extract key polaron properties—the energy, quasiparticle residue, and effective mass—using trap modulation and Bragg spectroscopy. Our measurements are well captured by a microscopic T-matrix approach and quantum Monte Carlo simulations, revealing deviations from mean-field predictions. In particular, we measure a significant enhancement of the polaron mass, with values exceeding twice the free-dimer mass. Our demonstration of a stable repulsive Bose polaron establishes a platform for studying impurity physics in low-dimensional and strongly correlated systems.

DOI: 10.1103/m5qj-j8bm

Subject Areas: Atomic and Molecular Physics, Condensed Matter Physics, Quantum Physics

I. INTRODUCTION

Polarons—quasiparticles formed by impurities interacting with a surrounding quantum medium—play a crucial role in understanding quantum many-body systems. Originally introduced by Landau and Pekar to describe electrons coupled to a crystal lattice [1], the polaron concept has since provided valuable insights into phenomena ranging from the phase diagram of superfluid helium mixtures [2] to the optical response of doped semiconductors [3], and the pairing mechanism underlying high-temperature superconductivity [4]. Despite its conceptual simplicity, the quantum impurity problem represents a paradigmatic many-body challenge, and a central question is how the quasiparticle picture evolves in the strongly correlated regime.

Ultracold atoms provide an ideal platform for studying polaron physics due to the ability to tune the atom-atom interactions [5] and prepare impurities in bosonic and fermionic mediums [6,7]. For both these Bose and Fermi polarons, it is now well established that the impurity spectrum features attractive and repulsive branches, where the impurities attract or repel the surrounding medium [6,7]. However, this scenario involves underlying attractive interactions where the physics of the attractive polaron is influenced by few-atom bound states [8–14], while the repulsive polaron is intrinsically unstable [9–12,14–17]. The situation is particularly severe for Bose polarons in the strongly interacting regime, since bosons tend to form clusters and are more susceptible to three-body losses [18,19]. As a result, experimental studies of repulsive polarons have so far been limited to transient regimes and it remains unclear whether the quasiparticle picture holds under strong repulsion [7].

*Contact author: hennning.moritz@uni-hamburg.de
†Contact author: cesar.cabrera@uni-hamburg.de

Published by the American Physical Society under the terms of the Creative Commons Attribution 4.0 International license. Further distribution of this work must maintain attribution to the author(s) and the published article's title, journal citation, and DOI.

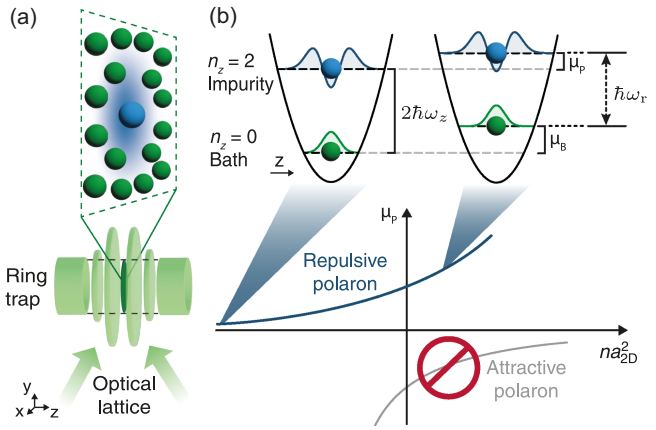


FIG. 1. Experimental realization of repulsive synthetic-spin polarons. (a) An impurity (blue) is immersed in a homogeneous 2D Bose-Einstein condensate (green). The atomic cloud is confined to a single 2D plane of a blue-detuned optical lattice in combination with a ring trap (box potential in the radial plane). (b) The eigenstates of the harmonic trapping potential along the z direction play the role of synthetic spins, allowing us to realize a 2D repulsive polaron. Here, the bath corresponds to a superfluid of density n in the ground state $n_z = 0$, while the impurity is created by populating a higher level such as $n_z = 2$. Without interactions, the energy $\hbar\omega_r$ to address this transition is $2\hbar\omega_z$, the harmonic oscillator level spacing. With increasing repulsion na_{2D}^2, $\hbar\omega_r$ exhibits an interaction shift arising from the difference between the bath chemical potential μ_B and the repulsive polaron energy μ_P. In contrast to previous Bose polaron realizations, there is no underlying attractive branch.

Here, we experimentally realize a stable repulsive Bose polaron in the strongly interacting regime, overcoming the intrinsic metastability observed in previous studies [10,11,14,17]. We focus on the two-dimensional (2D) geometry [Fig. 1(a)], where correlations are enhanced and striking phenomena are predicted, such as effective mass divergence and the breakdown of the quasiparticle picture [20–25]. Our approach employs bosonic Feshbach molecules consisting of pairs of fermions [26] which have a strong immunity against typical three-body decay due to the Pauli exclusion principle [27]. In addition, they feature repulsive interactions [27] with large tunability, allowing us to realize strongly repulsive superfluids. Simultaneously, the strong 2D confinement enables us to create impurities within the superfluid by exciting a small number of dimers from the ground state to an excited state of the trapping potential, with the quantum number n_z acting as a synthetic spin [Fig. 1(b)]. This mapping of impurity and bath into different vibrational states gives rise to a new class of quasiparticle which we term the *synthetic-spin polaron*, characterized by purely repulsive interactions and the absence of any underlying attractive branch. We access the polaron spectral function and extract the polaron quasiparticle properties using trap modulation spectroscopy and Bragg spectroscopy. Most notably, we measure the effective mass of the Bose polaron for the first time, observing values exceeding twice the bare mass of a noninteracting impurity, a hallmark of strong many-body dressing. Comparisons with quantum Monte Carlo (QMC) and T-matrix theories reveal pronounced beyond-mean-field (BMF) effects in a regime previously inaccessible.

II. EXPERIMENTAL SYSTEM

The experiments are performed in a homogeneous gas of bosonic dimers, each composed of two ^{6}Li fermions occupying the lowest two hyperfine states. To ensure the bosonic character of the system, we stay in the regime where the dimer size is smaller than the interparticle distance. The cloud is confined in a highly anisotropic geometry with a trapping frequency $\omega_z = 2\pi \times 11.4$ kHz along the vertical direction, and a uniform box potential providing horizontal confinement [28,29], as illustrated in Fig. 1(a). The typical temperatures measured after an adiabatic ramp to low interactions are $\tilde{T} \leq 0.02T_F$, where T_F is the Fermi temperature (further experimental details in Appendix A). We tune the interaction strength via a broad Feshbach resonance [28,29]. It is quantified using the dimensionless gas parameter na_{2D}^2, where n is the total 2D dimer density and the scattering length a_{2D} is obtained by mapping the 3D interaction between composite dimers [27] to the quasi-2D geometry [30]. The gas parameter also defines the dimensionless parameter $\ln(k_n a_{2D})$, which is commonly used to describe 2D systems, where $k_n = \sqrt{4\pi n}$ is the characteristic momentum scale. We note that in our scheme the underlying microscopic interaction potential between the $n_z > 0$ impurity and the bath particles is the same as that between particles in the bath, with differences in the effective interactions being due to the transverse overlaps O_{n_z} (see Appendix B). Specifically, the impurity-bath interactions are typically reduced, with an effective 2D scattering length given by $k_n a_{2D,n_z} = (k_n a_{2D})^{1/O_{n_z}}$. This effect is conceptually similar to the scenario of ^{3}He impurities in superfluid ^{4}He [2], where the larger volume occupied by the lighter ^{3}He atom yields different effective interactions despite the same underlying interaction potential.

III. POLARON CHARACTERIZATION

A. Trap modulation spectroscopy

To probe the properties of a 2D Bose polaron, we measure its spectral response using trap modulation spectroscopy [31], which we show (see Appendix D) is equivalent to injection radio-frequency (rf) spectroscopy widely used in Bose polaron experiments in the case of a BEC [11,14]. Specifically, we modulate the vertical trapping frequency as $\omega_z(t) = \omega_z[1 + \alpha \sin(\omega_m t)]$, with modulation frequency ω_m and a small amplitude of $\alpha \leq 0.5\%$. This transfers a small fraction of dimers from the superfluid

($n_z = 0$) into the $n_z = 2$ harmonic oscillator level, acting as impurities populating the repulsive polaron branch. Following the excitation, a 20-ms hold time allows for collisions between impurities and the bath, resulting in energy redistribution and measurable heating (see Appendix D). The heating rate of the condensate is directly linked to the zero-momentum spectral function $A_2(\omega)$ for the $n_z = 2$ impurities (see Appendix D):

$$\frac{dE}{dt} \propto A_2(\omega_{\mathrm{m}} + \mu_{\mathrm{B}}). \tag{1}$$

This mapping demonstrates that trap modulation provides the spectral information of injected $n_z = 2$ impurities (polarons) into the condensate, and consequently that eigenstates of the trap can be exploited as synthetic spin. Note that this differs from previous experiments on trapped motional states in a quantum bath, which only explored weak interactions and required a different species of atom for the impurity [32,33].

Experimentally, we quantify the heating rate via the response function $R(\omega_{\mathrm{m}}) = 1 - C(\omega_{\mathrm{m}})/C(0)$. Here, $C(\omega_{\mathrm{m}})$ corresponds to the amplitude of low-momentum atoms, determined from the bimodal momentum distribution after time-of-flight (TOF) imaging. It is normalized by the unperturbed amplitude $C(0)$, such that $R(\omega_{\mathrm{m}})$ becomes nonzero when the modulation is resonant with an excitation. In the limit of small energy transfers, $R(\omega_{\mathrm{m}})$ is proportional to dE/dt, and according to Eq. (1), proportional to the polaron spectral function.

B. Energy

In Fig. 2(a), we show $R(\omega_{\mathrm{m}})$ as a function of the gas parameter. The excitation spectrum features a well-defined resonance across the entire interaction range, clearly below the bare transition $2\omega_z$ (dashed line). Additionally, a second mode appears at $2\hbar\omega_z$ for larger interactions, corresponding to thermal dimers and unpaired fermions that are parametrically heated. The interaction shift $\Delta = \hbar(\omega_{\mathrm{r}} - 2\omega_z)$, shown in Fig. 2(b), consists of two contributions: the chemical potential of the bath μ_{B}, representing the energy lost by removing a particle from the condensate, and the polaron energy μ_{P}, corresponding to the energy required to add an impurity into the system. Their difference yields the total energy shift: $\Delta = \mu_{\mathrm{P}} - \mu_{\mathrm{B}}$. Notably, due to the reduced spatial overlap between the impurity and the bath, we find that $\mu_{\mathrm{B}} > \mu_{\mathrm{P}}$, and hence $\Delta < 0$, even though the polaron is repulsive, $\mu_{\mathrm{P}} > 0$. Since μ_{B} has been previously calculated in weakly interacting 2D Bose gases [34–36], our measurement of Δ provides experimental access to the polaron energy μ_{P} (see Appendix C), revealing the many-body dressing of the impurity.

To test the validity of the polaron description, we compare our experimental results with two complementary theoretical approaches—diffusion Monte Carlo simulations (denoted as QMC) and a T-matrix-based polaron theory—

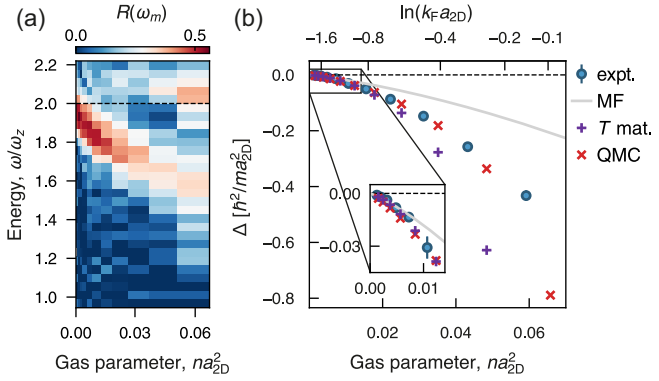


FIG. 2. Polaron energies from trap modulation spectroscopy. (a) Response $R(\omega_{\mathrm{m}})$ measured via trap modulation spectroscopy. A well-defined mode is visible, corresponding to the creation of polarons in the $n_z = 2$ state. (b) Energy shift Δ, extracted from Lorentzian fits to the spectra shown in (a). The error bars of the experimental data corresponding to the standard deviation σ from the fits are small compared to the symbol size. A comparison with QMC theory shows excellent agreement up to $na_{2D}^2 \lesssim 0.05$ in the strongly interacting regime. Both T-matrix and QMC theories deviate for large interactions, where the details of the scattering potential become relevant, while MF theory fails already for moderate interactions. For small interactions, all theories agree well with the experiment (inset).

which highlight different aspects of the interactions (see Appendixes F and G). Specifically, the T-matrix theory precisely captures the low-energy two-body scattering between an $n_z > 0$ impurity and an $n_z = 0$ bath particle, including the possibility of decay of the impurity, but it neglects interactions within the medium and multiple excitations of the medium, as well as the finite range of the interaction potential (set by the dimer size). Conversely, the QMC method captures finite range effects and higher order correlations, but it neglects decay mechanisms and treats the $n_z = 2$ impurity as distinct from the bath particles, as in the standard polaron scenario. Neither theory treats the constituent fermionic particles forming the bosons, which is reasonable since the mean interparticle distance exceeds the dimer size.

The remarkable agreement seen in Fig. 2(b) for $na_{2D}^2 \lesssim 0.02$ between both theories and the experiment indicates that the polaron picture indeed applies to excitations of the transverse degrees of freedom and that the resulting description is universal, as it does not depend on the precise details of the interaction potential. At stronger interactions, discrepancies between theories and experiment emerge, which can be attributed to missing correlations in the T-matrix theory as well as the growing importance of the microscopic details. First, the QMC description models the dimers as hard spheres, an approximation that becomes inaccurate when the dimer diameter a_{3D} becomes comparable to the oscillator length l_z. Additionally, the gas enters the strongly correlated regime

when $na_{2D}^2 \sim 0.1$, which, for reference, is near the crystallization point predicted for hard disks at $na_{2D}^2 \approx 0.18$ [37]. Finally, the composite nature of the bath particles becomes relevant when the dimer size becomes comparable to the distance between dimers. For comparison, we also include a mean-field (MF) prediction (gray line), which estimates the energy shift based only on the reduced spatial overlap between $n_z = 2$ and $n_z = 0$ harmonic oscillators. This trivial MF approach neglects many-body correlations intrinsic to polaron formation and breaks down in the intermediate to strongly interacting regime.

C. Lifetime and quasiparticle residue

Having established the energy shift Δ as a proxy for the polaron energy, we now turn to two additional quasiparticle properties encoded in the spectral response: the lifetime and the quasiparticle residue, directly related to the spectral width and weight, respectively. As shown in Fig. 3(a), the spectral response shows a well-defined resonance visible throughout the strongly interacting regime, indicating the remarkable stability of the repulsive polaron branch in our system.

The inset in Fig. 3(a) shows how the full width at half maximum (FWHM) γ (inverse lifetime) extracted from a Lorentzian fit remains narrow across the explored region, normalized by the characteristic energy scale $E_n = \hbar^2 k_n^2/2m$. This is in contrast to previous experiments [10,11,14], where the molecule-hole continuum was also observed. The difference arises from a fundamental distinction in how the repulsive branch is engineered. Unlike previous experiments, where the repulsion stems from the presence of an underlying molecular state [38], our scheme uses the residual repulsion between stable bosonic dimers [27,39]. Therefore, the bound state responsible for the instability of the repulsive branch does not exist. This key feature not only leads to a robust, long-lived repulsive branch but also enables direct comparison with variational and quantum Monte Carlo descriptions, which typically neglect bound states [40,41].

We additionally compare the width with the prediction from T-matrix theory. Within this theory, the width originates from collisions where the $n_z = 2$ impurity scatters into high-momentum states in the $n_z = 0$ level. We find that in order to match the experiment, we need to include a constant offset of $\hbar\gamma_{\mathrm{offset}}/E_n = 0.475 \pm 0.015$. Experimentally, this offset cannot be explained by the frequency resolution set by the driving duration, which contributes to only ~10% of the total width. The most plausible explanation is temperature effects. Those are not covered by our theoretical descriptions and require further investigation.

The second quantity encoded in the spectral function is the quasiparticle residue Z, which quantifies how much of the original undressed particle remains after interaction with the bath: $Z = 1$ for a free particle, while $Z < 1$ indicates many-body dressing [7]. In the spectral function, Z corresponds to the integrated weight of the resonance [shaded area in Fig. 3(a)], which we extract from the Lorentzian fits. The resulting values of Z, normalized to the weakest interaction strength ($na_{2D}^2 \sim 0.001$), are displayed in Fig. 3(b), showing excellent agreement with our predictions. The gradual decrease for larger interactions signals the many-body dressing by the bath, while upholding the validity of the quasiparticle picture ($Z > 0$).

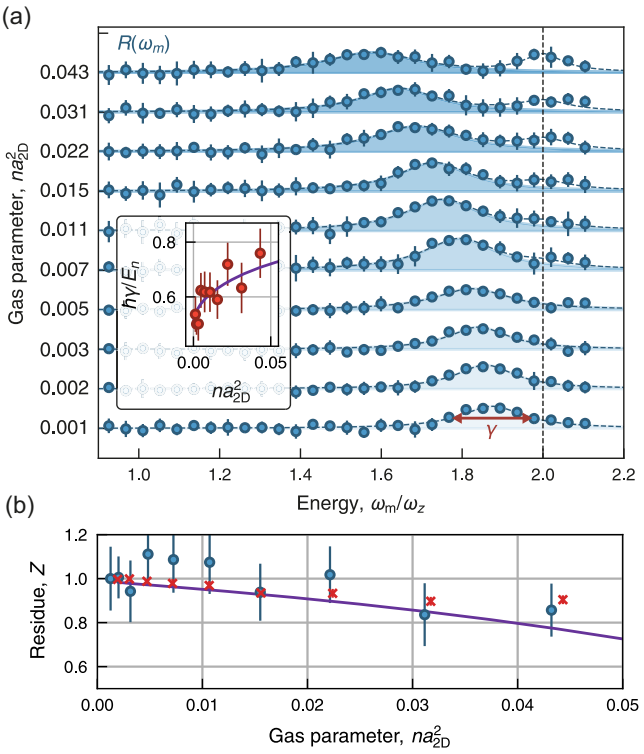


FIG. 3. Spectral function at different interaction strengths. (a) Ridge plot showing the response for different na_{2D}^2, directly connected to the spectral function $A_2(\omega_m + \mu_B)$. The error bars correspond to the shot-to-shot standard deviation of the response. From Lorentzian fits (blue dashed lines), the full width at half maximum γ is extracted (inset), as well as the integral, shown as blue shaded areas, which determines the quasiparticle residue Z. As impurity-bath interactions increase, the spectral response shifts and broadens, reflecting strong correlations with the medium. A comparison of the width with T-matrix theory plus a constant offset (purple line) shows good agreement. (b) Quasiparticle residue Z, quantifying the overlap between the dressed polaron and a noninteracting particle. The error bars correspond to the standard deviation from the fit. For increasing na_{2D}^2, the extracted Z (blue circles) steadily decreases, signaling enhanced dressing by the bath, which is supported by QMC (red crosses) and T-matrix (purple line) calculations.

D. Effective mass

In addition to the energy shift Δ, spectral width γ, and quasiparticle residue Z, we measure the effective polaron mass m^*. This quantity characterizes the mobility of the

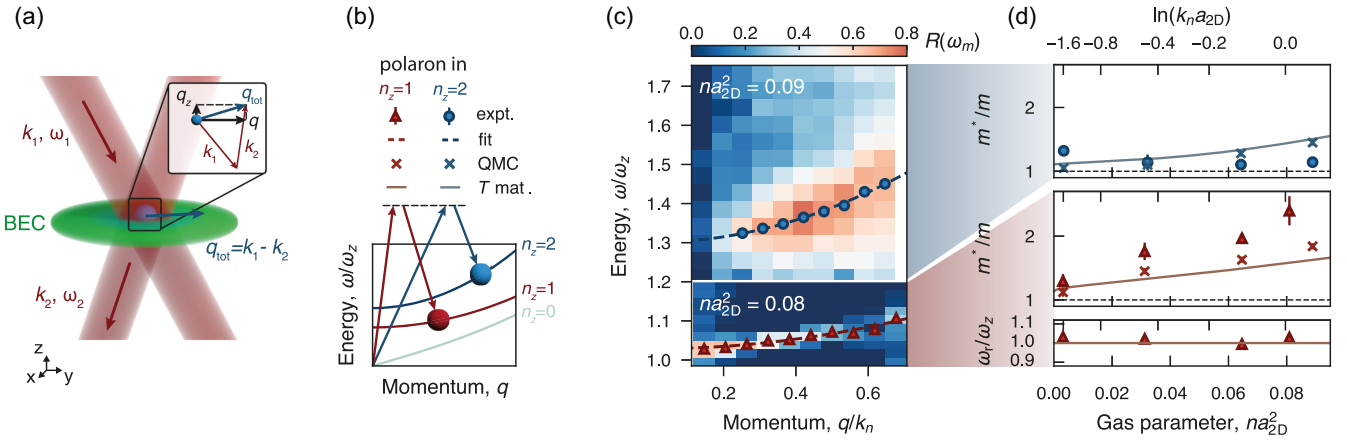


FIG. 4. Effective mass of the $n_z = 1$ and $n_z = 2$ polaron. (a) Creation of a polaron via Bragg spectroscopy: By overlapping two beams onto the atoms, a selected energy of $\omega_m = \omega_1 - \omega_2$ and momentum $\mathbf{q}_{tot} = \mathbf{k}_1 - \mathbf{k}_2$ can be transferred. Slightly tilting the beams allows for excitations into the $n_z = 1$ and $n_z = 2$ impurity states due to a small transverse momentum $q_z \ll q_{tot}$ imparted in addition to an in-plane momentum $q \approx q_{tot}$ (inset). (b) Bragg spectrum of a bosonic superfluid, displaying the phonon ($n_z = 0$) and the impurity modes ($n_z = 1$ and $n_z = 2$). The inverse of the curvature of the impurity dispersion directly gives the effective mass m^*. (c) Bragg spectra for the $n_z = 1$ (lower panel) and $n_z = 2$ (upper panel) in the strongly interacting regime. The energies $E_P(q)$ and the standard deviation for the error bars are extracted from Lorentzian fits to the momentum slices, including the quadratic fits, and are overlaid. (d) Effective masses extracted from the quadratic fits to the Bragg spectra, including a comparison with QMC and T-matrix theory. The error bars for the experimental data are obtained via repeatedly fitting to a bootstrapped dataset and taking the standard deviation of the values for the effective mass. The bottom panel shows the zero-momentum energies $\omega_r = E_P(q = 0)$ for $n_z = 1$ extrapolated from the fit. Remarkably, the energy shift from the bare transition remains zero for all gas parameters na_{2D}^2 due to symmetry.

impurity and follows the dispersion relation $E_P(q) = E_P(0) + \hbar^2 q^2/2m^*$. We measure $E_P(q)$ using Bragg spectroscopy, where a two-photon process transfers a precise energy $\hbar\omega_m$ and in-plane momentum $\hbar q$ to the impurity [see Fig. 4(a)]. As described in our previous experiments [29,42], the interference of two far-detuned laser beams creates a running-wave optical lattice with tunable spacing. It is important to note that coupling into the n_z states requires a small out-of-plane momentum component q_z (see Appendix E), which we introduce by slightly tilting the Bragg beams (q_{tot}) relative to the atomic plane ($q_z \approx 0.05 q_{tot}$); see inset in Fig. 4(a). As shown in Fig. 4(b), this off-axis Bragg excitation allows transitions to $n_z = 1$ and $n_z = 2$, as the matrix elements between harmonic oscillator states are not constrained by parity [43]. Using the detection protocol introduced for Δ in Fig. 2, we measure the momentum-resolved resonance frequency.

A typical Bragg spectrum in the strongly correlated regime is shown in Fig. 4(c). This spectrum combines two datasets for the $n_z = 1$ (bottom) and $n_z = 2$ (top) impurity. For each momentum slice, $E_P(q)$ is determined individually, allowing us to fit a quadratic dispersion [44], which gives the effective mass. For comparison, in our theory models, we extract m^* as follows: In QMC calculations, the effective mass is obtained from the imaginary-time diffusion coefficient assuming distinguishable impurities. Independently, using T-matrix theory, we extract the effective mass from the impurity self-energy, which determines the momentum-resolved spectral function $A_{n_z}(q, \omega)$ (see Appendix F).

The resulting effective masses for the $n_z = 1$ and $n_z = 2$ polaron branches are shown in Fig. 4(d) for a wide range of na_{2D}^2. In the weakly interacting regime, the measured effective masses for both $n_z = 1$ and $n_z = 2$ are close to $2m_{Li}$, consistent with the picture of nearly free dimers moving through the bath. However, at strong coupling, the two branches noticeably differ. For the $n_z = 1$ impurity, we observe a pronounced increase in the effective mass, exceeding twice the bare dimer mass for our strongest bath-impurity coupling, which is much larger than the effective masses observed previously for Fermi polarons [9,16,45,46]. Both T-matrix and QMC predictions qualitatively capture this increase, confirming this feature as a clear signature of many-body dressing arising from the repulsive dimer-dimer interactions and the absence of an underlying bound state [27].

By contrast, we measure a nearly constant effective mass for the $n_z = 2$ polaron. Although m^* for $n_z = 2$ is expected to be smaller than for $n_z = 1$ due to its reduced overlap with the bath, the absence of any noticeable increase with stronger bath-impurity coupling is unexpected. In both datasets, we verified that no systematic energy shifts appear when varying the driving strength, and that the effective mass from the quadratic fit does not change when removing the highest momenta from the data, ruling out nonquadratic contributions. The qualitative difference potentially stems from the fact that the $n_z = 2$ impurity can decay into the

bath, whereas the $n_z = 1$ impurity is protected by parity symmetry. This is supported by their respective widths in Fig. 4(c). Moreover, only the former exhibits a strong broadening at large momenta, a feature not captured by either theory, possibly because it requires decay processes involving multiple excitations of the medium.

While the effective mass reveals strong interaction effects for the $n_z = 1$ impurity, the energy shift shows a remarkably different behavior. The bottom panel of Fig. 4(d) shows the extrapolated zero-momentum energies $E_{\mathrm{P}}(0) = \Delta_{n_z=1} + \hbar\omega_z$ from Bragg spectroscopy, extracted from the quadratic fit. Surprisingly, there is no deviation from the bare transition across the full interaction range. This striking result stems from the parity symmetry of the trapping potential: Since there are no odd-parity pairwise interactions, the $n_z = 1$ excitation can only go into the center-of-mass motion of the gas without changing its properties. This is in analogy with Kohn's theorem. Within the impurity picture, this property appears as a cancellation between the factor of 2 due to impurity-bath exchange *during scattering* (which is incorporated into our T-matrix approach) and the factor of $1/2$ arising from the reduced spatial overlap between $n_z = 1$ and $n_z = 0$ wave functions. The resulting vanishing interaction energy shift thus highlights a subtle manifestation of quantum indistinguishability. Furthermore, the observed exchange process is a property of the impurity-bath interactions that exists even at $T = 0$. It is thus different from the exchange of thermal bosons that takes place in the driving transition in measurements of clock shifts in a thermal Bose gas [47,48].

IV. CONCLUSION AND OUTLOOK

In conclusion, we have engineered a stable Bose polaron in 2D and measured the key properties from the weakly to the strongly interacting regime. Those include the polaron energy and the quasiparticle residue, finding excellent agreement with QMC predictions and T-matrix calculations. Furthermore, we determined the effective mass via Bragg spectroscopy, showing a significant increase in the effective polaron mass and absence of the energy shift Δ associated with the $n_z = 1$ polaron, due to bosonic statistics. Our work demonstrates how the internal states of the confining potential can be exploited as pseudospins, enabling momentum-resolved spectroscopy without relying on rf or Raman transitions. We term this long-lived quasiparticle the synthetic-spin polaron. Next steps include extending this approach to finite temperatures, which will enable the exploration of how thermal fluctuations affect polaron stability and mobility, thereby deepening our understanding of quasiparticles in low-dimensional Bose systems. While this work focuses on the bosonic regime, our polaron mapping, based on internal states, can be extended to imbalanced Fermi gases [49], enabling exploration of the crossover between Bose and Fermi polarons within the same experimental platform.

ACKNOWLEDGMENTS

We gratefully acknowledge fruitful discussions with L. Ardila, F. Scazza, J. Arlt, G. Bruun, P. Massignan, C. Eigen, and H. Biss. J. L. and M. M. P. are supported through Australian Research Council Discovery Project No. DP240100569 and Future Fellowship No. FT200100619, respectively. C. R. C. acknowledges financial support from the Maria de Maeztu excellence unit Grant No. CEX2023-001318-M funded by MICIU/AEI/10.13039/501100011033, the Xunta de Galicia (CIGUS Network of Research Centres), and the EU through the Galicia Feder 2021-2027 Program. J. B. and G. E. A. acknowledge financial support from Ministerio de Ciencia e Innovación MCIN/AEI/10.13039/501100011033 (Spain) under Grant No. PID2023-147469NB-C21. This work is supported by the Deutsche Forschungsgemeinschaft (DFG, German Research Foundation) in the framework of SFB-925—Project No. 170620586—and the Cluster of Excellence "CUI: Advanced Imaging of Matter"—EXC 2056—Project No. 390715994 and co-financed by ERDF of the European Union and by "Fonds of the Hamburg Ministry of Science, Research, Equalities and Districts" (BWFGB).

R. H. and C. R. C. performed the experiments and analyzed the data. J. L. and M. M. P. developed the T-matrix theory and the linear-response formalism. G. E. A. and J. B. performed the QMC simulations. C. R. C. and H. M. supervised the work. All authors contributed to the interpretation of the results and to the preparation of the manuscript.

The authors declare no competing interests.

DATA AVAILABILITY

The datasets supporting this study are available at Ref. [50].

APPENDIX A: EXPERIMENTAL DETAILS

1. Preparation

We prepare the 2D superfluid by evaporating a balanced two-component Fermi mixture of ^{6}Li in the lowest two hyperfine states $|F = 1/2, m_F = \pm 1/2\rangle$ close to the Feshbach resonance at 832 G. This is achieved by using an attractive, oblate dipole trap (squeeze trap) at a wavelength of $\lambda = 1064$ nm. A magnetic field gradient deterministically spills the gas to a desired number of atoms, fluctuating less than 5% in between experimental cycles. The atoms are then transferred to the repulsive box potential used for the main experiment. First, the magnetic field is ramped to the low-interacting bosonic regime far below the Feshbach resonance (750 G $\rightarrow 3516a_0$, with the Bohr radius a_0), which shrinks the cloud for an efficient transfer into the box potential. Subsequently, the repulsive dipole traps for the 2D homogeneous box are switched on,

consisting of the ring and accordion, both at $\lambda = 532$ nm. The ring is projected through the microscope and radially confines the atoms within a diameter of ∼90 μm. For the 2D confinement, we employ a vertical accordion lattice, which is created by overlapping two beams from the side at an angle which can be continuously tuned between 1.5° and 13°, leading to trapping frequencies ranging from $\omega_z = 2\pi \times 0.8$ kHz up to $2\pi \times 11.5$ kHz, respectively. After loading atoms into the open accordion, it is compressed to $\omega_z = 2\pi \times 11.4$ kHz, leaving a superfluid in the 2D regime. To achieve our final temperatures, a last evaporation is performed by lowering the ring power. For efficient evaporation, we utilize the anticonfinement of the accordion trap, which is typically canceled out by the coils that create the magnetic field used to tune the interactions. A different set of coils in a Helmholtz configuration generates a homogeneous magnetic field at the same field strength as during evaporation (832 G), leaving the accordion's anticonfinement in place. Therefore, during evaporation, the hot atoms outside the ring are actively pushed away, leaving a clean superfluid at temperatures $\tilde{T}/T_F \leq 0.02$ (more details on the temperature measurement in Appendix A 2). After this evaporation, we ramp the magnetic field to reach the interactions in the main text.

All measurements are performed at a density of $n \approx 0.9\ \mu\text{m}^{-2}$ such that we remain in the 2D regime with $E_F < \hbar\omega_z$, where $E_F \approx h \times 9.5$ kHz is the Fermi energy, which is an upper bound for the chemical potential in the BEC-BCS crossover.

2. Measuring the temperature

To extract the temperatures of the prepared samples, we use the thermal wings of the momentum distribution. We access this distribution via a $T/4$ time-of-flight measurement: After a magnetic field ramp to low interactions at $B = 750$ G, where $na_{2D}^2 = 6 \times 10^{-4}$ or $\ln(k_F a_{2D}) = -2.5$, we switch off the optical trapping potentials and exploit the residual radial confinement of 28 Hz from the magnetic field. After a quarter of a period $T/4 = 9$ ms, the momentum space maps to real space and can be imaged via standard absorption imaging [28].

However, because the superfluid is strongly confined along the imaging axis prior to switch-off, the cloud rapidly expands beyond the microscope's depth of field, distorting the momentum distribution. We resolve this issue by slightly tilting the imaging beam [see Fig. 5(a)] such that the z axis is partially mapped to the y axis of the density images, resulting in the elongated shape shown in Fig. 5(b). The center, as indicated by the dashed lines, corresponds to the atoms in focus, showing the actual momentum distribution, while the atoms farther above and below are out of focus.

To extract the temperature, we average over 50 density images, take a vertical sum with a width of 6 pixel, and fit a bimodal distribution [see Fig. 5(c)]. The bimodal fit

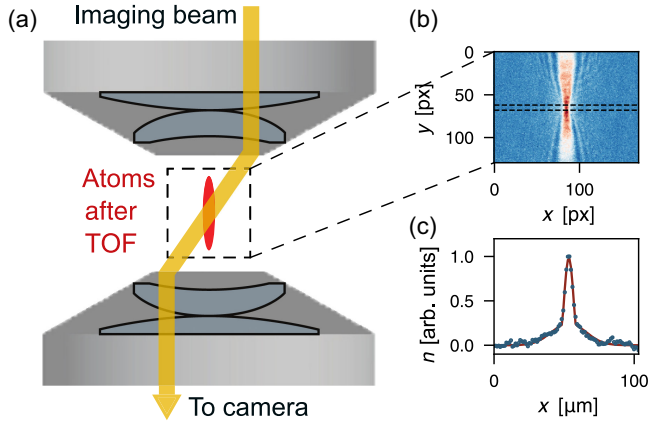


FIG. 5. Tilted imaging. (a) Sketch of tilted imaging. After TOF expansion, the atoms vertically expand due to the previous confinement. We perform absorption imaging using a tilted beam to avoid artifacts caused by out-of-focus atoms. We can therefore extract the response and temperature from a small in-focus region in the images. (b) An average of 50 absorption images taken with a tilted imaging beam. The central region indicated by the dashed lines shows no diffraction fringes. The atoms above and below this region are out of focus. (c) Momentum distribution obtained from the vertical sum of the region between the dashed lines in (b). The red line is a bimodal fit used to extract the temperature.

combines a parabolic term for the condensate and a Boltzmann distribution, with the temperature given by the thermal wings.

To be consistent with the spectroscopic measurements, we use the same experimental sequences, with the same hold times and interaction parameters, but with the driving disabled. In trap modulation spectroscopy, we keep the trap frequency constant, whereas in Bragg spectroscopy, we project a static lattice ($\omega_m = 0$). Identical to the response measurements, we then adiabatically ramp the field to 750 G ($na_{2D}^2 \approx 6 \times 10^{-4}$) for the $T/4$ time-of-flight procedure. Therefore, the temperature is known only at low interactions and not the na_{2D}^2 given in the spectra. The entropy stays constant, however, since our interaction ramps are adiabatic.

For all measurements performed, the temperatures are at $\tilde{T}/T_F \leq 0.02$.

3. Extraction of the response

For both spectroscopy measurements—trap modulation and Bragg spectroscopy—we extract the response by accessing the momentum distribution via $T/4$ TOF, as explained for the temperature measurement in Appendix A 2. When driving a resonance, the superfluid heats up, resulting in a reduced condensate density, which manifests as a reduction of the low-momentum peak in the momentum distribution.

Comparing the peak densities of the low-momentum peaks of the unperturbed system $C(0)$ with the driven

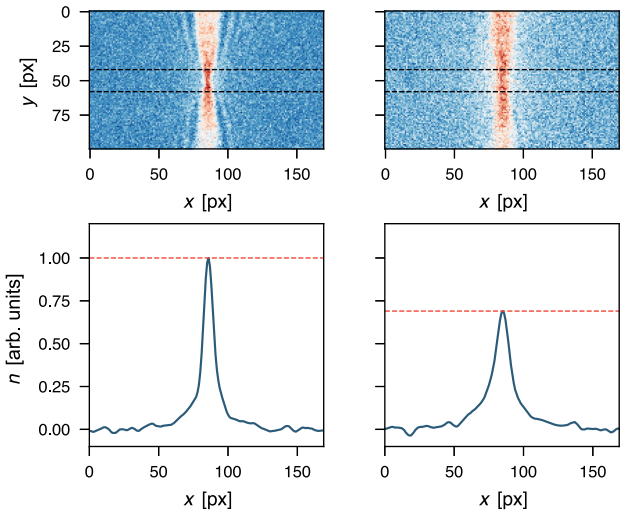


FIG. 6. Extraction of the response. Density images after a 9-ms $T/4$-TOF expansion for a system before (left) and after (right) resonant modulation. The imaging is slightly tilted to avoid fringes caused by atoms that have expanded out of focus from entering the central region. The smoothed horizontal slices from the sum between the black dashed lines are shown in the lower panels. A clear condensate peak is visible for both slices, but with different maximum values (red dashed lines).

system $C(\omega_{\mathrm{m}})$ then allows us to extract the response [29]:

$$R(\omega_{\mathrm{m}}) = 1 - \frac{C(\omega_{\mathrm{m}})}{C(0)}. \tag{A1}$$

We extract the peak densities $C(\omega_{\mathrm{m}})$ by taking a vertical sum of the densities in between the dashed lines shown in the top panels of Fig. 6 (16 pixel wide), where no diffraction fringes are visible, and smoothing the distribution, shown in the bottom panels of Fig. 6. $C(\omega_{\mathrm{m}})$ corresponds to the maximum value (red dashed line) and is averaged over 10 images for each data point.

Close to a quasiparticle pole at ω_r, the spectral function for a single impurity takes the form

$$\begin{aligned} A(\omega) &= -\frac{1}{\pi}\mathrm{Im}\frac{Z}{\omega - \omega_r + i\gamma} \\ &= \frac{Z\gamma/\pi}{(\omega-\omega_r)^2 + \gamma^2}. \end{aligned} \tag{A2}$$

Therefore, to extract the energy shift Δ from the bare transition [main text Fig. 2(b)], the full width at half maximum γ [main text Fig. 3(a)] and the quasiparticle residue Z [main text Fig. 3(b)], we perform a Lorentzian fit of $R(\omega_{\mathrm{m}})$. These fits are shown in Fig. 3(a) in the main text and directly give the resonance frequency ω_{r} used to calculate Δ. We normalize all Lorentzians with the value at the lowest interaction, since $Z = 1$ for $na_{2\mathrm{D}}^2 = 0$.

APPENDIX B: QUASI-TWO-DIMENSIONAL INTERACTION PARAMETERS

The starting point of our experiment is a Bose-Einstein condensate of bosonic dimers composed of fermionic atoms in the two lowest hyperfine states of ^{6}Li. We work in the universal regime where, in the absence of any transverse confinement, the binding energy of dimers is directly linked to the 3D s-wave atom-atom scattering length a_s via $\varepsilon_B = \hbar^2/m_f a_s^2$ ($m_f = m/2$ is the fermion mass). Furthermore, the dimer-dimer scattering length $a_{3\mathrm{D}}$ is [27]

$$a_{3\mathrm{D}} = 0.6 a_s. \tag{B1}$$

Note that, even though the dimers are extended objects of size $\sim a_{3\mathrm{D}}$, the dimer-dimer scattering amplitude only has a small effective range $r_{3\mathrm{D}} = 0.13 a_s$ [51]. Thus, in a quasi-2D geometry with transverse confinement frequency ω_z it is a reasonable assumption to treat the dimers as pointlike objects as long as $\varepsilon_B \gtrsim \hbar\omega_z$.

To arrive at the effective scattering properties in the confined geometry, we use the formalism of Ref. [30] (see also Refs. [52,53]). Here, the two-body scattering amplitude (or scattering T matrix) in the low-energy limit has the universal form,

$$\mathcal{T}(E) = \frac{4\pi\hbar^2}{m}\frac{1}{\ln(\hbar^2/m a_{2\mathrm{D}}^2 E) + i\pi}, \tag{B2}$$

where the effective 2D dimer-dimer scattering length is related to the 3D parameters via

$$a_{2\mathrm{D}} = l_z\sqrt{\frac{\pi}{B}} e^{-\sqrt{\pi/2}\, l_z/a_{3\mathrm{D}}}, \tag{B3}$$

with $B \approx 0.905$ [30,52]. The interactions between a dimer in the $n_z = 0$ BEC and an impurity dimer in either the $n_z = 1$ or the $n_z = 2$ level are distinct from those between $n_z = 0$ dimers due to the different spatial overlaps of the transverse wave functions. To see this, we first consider the simplest regime where $a_{3\mathrm{D}} \ll l_z$. Since in this case the dimer-dimer interactions are of much shorter range than the transverse harmonic confinement, the effective interactions are simply reduced by a factor

$$O_{n_z} = \frac{\int dz |\varphi_{n_z}(z)|^2 |\varphi_0(z)|^2}{\int dz |\varphi_0(z)|^4} = \begin{cases} \frac{1}{2} & n_z = 1 \\ \frac{3}{8} & n_z = 2. \end{cases} \tag{B4}$$

Using Eq. (B2), this allows us to arrive at an effective low-energy scattering length $a_{2\mathrm{D},n_z}$ acting between a majority boson and an impurity in the $n_z = 1$ or 2 level. Specifically, for a small collision energy $E = \hbar^2 k^2/m$, we have

$$\frac{1}{\ln(1/k^2a_{2D,n_z}^2)} = O_{n_z}\frac{1}{\ln(1/k^2a_{2D}^2)}, \tag{B5}$$

where, at sufficiently low energy, we can neglect the term $i\pi$. This yields

$$ka_{2D,n_z} = (ka_{2D})^{1/O_{n_z}}. \tag{B6}$$

Note that the fact that the impurity is in an excited level combined with the logarithm appearing in Eq. (B2) means that this relationship explicitly depends on the energy scale at which the scattering physics is probed. This energy scale will typically be set by k_n.

Our two theories treat the interactions between impurities and medium particles slightly differently, including the processes by which particles scatter into other levels of the transverse confinement. See the discussions in Appendixes F and G below.

APPENDIX C: POLARON ENERGIES

The energy shift measured via trap modulation spectroscopy is given by the polaron energy μ_P and the chemical potential of the bath μ_B, such that $\Delta = \mu_P - \mu_B$, as explained in the main text. This protocol removes a dimer from the bath and places it in the $n_z = 2$ state. To extract μ_P, we have to make assumptions about the bath chemical potential. Here we compare the following predictions.

(1) The chemical potential from our QMC calculations $\mu_{B,QMC}$.

(2) The mean-field prediction of 2D bosons from Ref. [34] corresponding to

$$\mu_{B,MF} = \frac{4\pi\hbar^2 n/m}{|\ln na_{2D}^2|}. \tag{C1}$$

(3) A beyond-mean-field correction to $\mu_{B,MF}$ from Ref. [35], resulting in

$$\mu_{B,BMF} = \frac{4\pi\hbar^2 n/m}{|\ln na_{2D}^2| + \ln|\ln na_{2D}^2| + C_1 + \frac{\ln|\ln na_{2D}^2| + C_2}{|\ln na_{2D}^2|}}, \tag{C2}$$

with coefficients

$$C_1 = -\ln\pi - 2\gamma - 1 = -3.3,$$
$$C_2 = -\ln\pi - 2\gamma + 2 = -0.3.$$

Here, $\gamma \simeq 0.577$ is Euler's constant.

A comparison of the different chemical potentials is shown in Fig. 7(a), and resulting polaron energies μ_P in Fig. 7(b) when adding μ_B to the measured energy shift Δ_{expt} from the experiment. Since our QMC theory agrees well with the results for $na_{2D}^2 < 0.06$ [see Fig. 2(b) in the main text], we expect the predicted chemical potentials to be close to the actual values for this regime. For larger interactions, the details of the scattering potential become relevant and the predictions for $\mu_{B,QMC}$ unreliable. The included BMF theory replicates these results. For completeness, we also included the 2D hard-core MF prediction $\mu_{B,MF}$, used in the main text, which clearly underestimates the chemical potential, leading to the prediction of negative polaron energies as a consequence. We therefore expect $\mu_{B,QMC}$ to be the most reliable prediction.

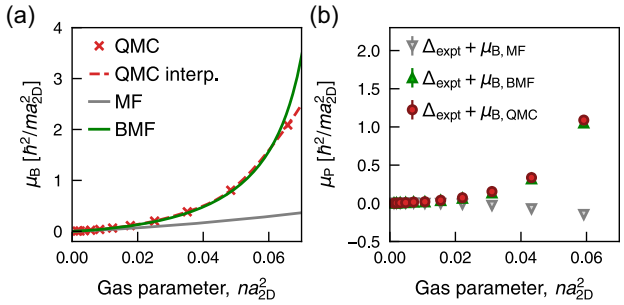


FIG. 7. Comparison with various chemical potentials. (a) Comparison of different predictions for the chemical potential μ_B of the bath (see text). (b) Polaron energy $\mu_P = \Delta_{expt} + \mu_B$, using the chemical potentials μ_B from a and Δ_{expt} from Fig. 2 in the main text. Since the values for Δ_{expt} lie at different interactions than the QMC predictions, $\mu_{B,QMC}$ is taken from the cubic spline interpolation shown in (a). For $na_{2D}^2 < 0.06$ the BMF and QMC predictions are expected to yield good results. In contrast, $\mu_{B,MF}$ underestimates the chemical potential, clearly visible from the negative predicted polaron energy $\mu_{P,MF}$.

APPENDIX D: RELATIONSHIP BETWEEN TRAP MODULATION SPECTROSCOPY AND POLARON SPECTRAL FUNCTION

In order to promote dimers to excited transverse levels, we modulate the transverse potential according to

$$V_\perp(z) = \frac{1}{2}m\omega_z^2 z^2[1 + \alpha\sin(\omega_m t)]^2 \simeq \frac{1}{2}m\omega_z^2 z^2[1 + 2\alpha\sin(\omega_m t)], \tag{D1}$$

where the amplitude α of the modulation is small. This yields a time-dependent perturbation on the gas of dimers, which can be written as

$$\hat{V}_\Omega(t) = 2\Omega\sin(\omega_m t)\int d^3r z^2 \underbrace{\hat{\psi}^\dagger(\mathbf{r})\hat{\psi}(\mathbf{r})}_{\hat{n}(\mathbf{r})}, \tag{D2}$$

where $\Omega \equiv \frac{1}{2}m\omega_z^2\alpha$ and $\hat{\psi}^\dagger(\mathbf{r})$ creates a bosonic dimer at position $\mathbf{r}$.

Now we can define

$$\hat{c}_{\mathbf{k}n} = \int d^3 r e^{-i\mathbf{k}\cdot\mathbf{r}_\perp} \varphi_n^*(z)\hat{\psi}(\mathbf{r}), \tag{D3a}$$

$$\hat{\psi}(\mathbf{r}) = \sum_{\mathbf{k},n} e^{i\mathbf{k}\cdot\mathbf{r}_\perp} \varphi_n(z)\hat{c}_{\mathbf{k}n}, \tag{D3b}$$

where $\varphi_n(z)$ is the harmonic oscillator wave function and $\mathbf{r}_\perp = (x, y)$. Thus, we have

$$\hat{V}_\Omega(t) = 2\Omega \sin(\omega_{\mathrm{m}} t) \sum_{\substack{\mathbf{k},n \\ m\geq n}} W_{nm}\left(\hat{c}^\dagger_{\mathbf{k}m}\hat{c}_{\mathbf{k}n} + \mathrm{H.c.}\right), \tag{D4}$$

with the coefficients

$$W_{nm} \equiv \int_{-\infty}^{\infty} dz \varphi_n^*(z) z^2 \varphi_m(z) = \begin{cases} \frac{2n+1}{2} l_z^2 & m = n \\ \frac{\sqrt{(n+1)(n+2)}}{2} l_z^2 & m = n+2 \\ 0 & \text{otherwise,} \end{cases} \tag{D5}$$

when $m \geq n$. These coefficients determine the amplitude for transitions from harmonic oscillator level m to n. Here, and in the following, we set the system area and $\hbar$ to 1.

We now wish to determine the heating rate due to the trap modulation, i.e., $d\langle\hat{H}\rangle/dt$, where $\hat{H}$ is the unperturbed Hamiltonian, which in the Schrödinger picture is given by

$$\hat{H} = \sum_{\mathbf{k}n} \xi_{\mathbf{k}n} \hat{c}^\dagger_{\mathbf{k}n}\hat{c}_{\mathbf{k}n} + \hat{U}_{\mathrm{int}}, \tag{D6}$$

where $\xi_{\mathbf{k}n} = \mathbf{k}^2/2m + n\omega_z$, and $\hat{U}_{\mathrm{int}}$ describes the interactions. Note that we measure energies with respect to the zero-point energy in the trap. Thus, we have

$$i\frac{d\langle\hat{H}\rangle}{dt} = \langle\psi|U^\dagger(t)[\hat{H}, \hat{V}_\Omega(t)]U(t)|\psi\rangle, \tag{D7}$$

where $U(t)$ is the time evolution operator with respect to the full Hamiltonian $\hat{H} + \hat{V}_\Omega$, and $|\psi\rangle$ is the initial state. Now $[\hat{U}_{\mathrm{int}}, \hat{V}_\Omega] = 0$ since the interaction term is also a function of the density operator $\hat{n}(\mathbf{r})$. Thus, we just need to compute the commutator for the kinetic term, which yields

$$[\hat{H}, \hat{V}_\Omega(t)] = 4\Omega \sin(\omega_{\mathrm{m}} t)\omega_z \sum_{\mathbf{k},n} W_{n,n+2}\left(\hat{c}^\dagger_{\mathbf{k}n+2}\hat{c}_{\mathbf{k}n} - \mathrm{H.c.}\right). \tag{D8}$$

Finally, since $\hat{V}_\Omega$ is a perturbation, we expand the time evolution operator:

$$U(t) = U_0(t) - iU_0(t)\int_{-\infty}^{t} dt' U_0^\dagger(t')\hat{V}_\Omega(t')U_0(t'), \tag{D9}$$

where $U_0(t) = e^{-i\hat{H}t}$. Here we have assumed that we have turned on the weak drive $\hat{V}_\Omega$ in the distant past; hence the lower bound of the integral is $-\infty$. After some algebra, we then obtain the heating rate up to order Ω^2:

$$\frac{dE}{dt} = 8\Omega^2\omega_z \sin(\omega_{\mathrm{m}} t)\int_{-\infty}^{t} dt' \sin(\omega_{\mathrm{m}} t') \sum_{\substack{\mathbf{k},\mathbf{k}',n,n' \\ m\geq n'}} W_{n,n+2}W_{n'm}\left\langle\left[\left(\hat{c}^\dagger_{\mathbf{k}'m}(t')\hat{c}_{\mathbf{k}'n'}(t') + \mathrm{H.c.}\right), \left(\hat{c}^\dagger_{\mathbf{k}n+2}(t)\hat{c}_{\mathbf{k}n}(t) - \mathrm{H.c.}\right)\right]\right\rangle. \tag{D10}$$

To make further progress, we assume that the initial state features a condensate in the $n_z = 0$ level and we only consider the heating of this condensate (which is the case in the experiment). This allows us to make the replacement $\hat{c}_{\mathbf{0},0}(t) \simeq \sqrt{n_0}e^{-i\mu_{\mathrm{B}}t}$ with n_0 being the condensate density, which then gives

$$\frac{dE}{dt} \simeq 16\Omega^2 n_0\omega_z \sin(\omega_{\mathrm{m}} t)\int_{-\infty}^{t} dt' \sin(\omega_{\mathrm{m}} t')\left(2W_{02}W_{00}\mathrm{Re}[e^{i\mu_{\mathrm{B}}t}\sqrt{n_0}\langle\hat{c}_2(t)\rangle] + W_{02}^2\mathrm{Re}[e^{i\mu_{\mathrm{B}}(t-t')}\langle\hat{c}_2(t)\hat{c}_2^\dagger(t')\rangle]\right), \tag{D11}$$

where we have used the shorthand notation $\hat{c}_n(t) \equiv \hat{c}_{\mathbf{0},n}(t)$. The 2-0 cross term is independent of t' and averages to zero for frequencies $\omega_{\mathrm{m}} \gtrsim \omega_z$ that are fast compared to the timescale of the applied drive, as is the case in the experiment. Similarly, the last term simplifies when we use the fact that $\omega_z < \omega_{\mathrm{m}} \lesssim 2\omega_z$, such that the non-energy-conserving off-resonant terms are highly oscillatory and thus can be neglected; i.e., we apply the rotating wave approximation. This yields

$$\begin{aligned} \frac{dE}{dt} &\simeq 4\Omega^2 n_0\omega_z W_{02}^2 \mathrm{Re}\left[\int_{-\infty}^{t} dt' e^{i(\omega_{\mathrm{m}}+\mu_{\mathrm{B}})(t-t')}\left\langle\hat{c}_2(t)\hat{c}_2^\dagger(t')\right\rangle\right] \\ &= 4\Omega^2 n_0\omega_z W_{02}^2 \,\mathrm{Im}\underbrace{\left[\int_0^{\infty} dt e^{i(\omega_{\mathrm{m}}+\mu_{\mathrm{B}})t} i\left\langle\hat{c}_2(t)\hat{c}_2^\dagger(0)\right\rangle\right]}_{-G_2(\omega_{\mathrm{m}}+\mu_{\mathrm{B}})}. \end{aligned} \tag{D12}$$

Here, $G_2(\omega)$ corresponds to the retarded Green's function for the $n_z = 2$ impurity.

Finally, since the spectral function of an $n_z = 2$ impurity is $A_2(\omega) = -\operatorname{Im} G_2(\omega)/\pi$, we see that the heating rate is simply proportional to A_2:

$$\frac{dE}{dt} \propto n_0 A_2(\omega_{\mathrm{m}} + \mu_{\mathrm{B}}), \tag{D13}$$

where we have kept the condensate density n_0 as a reminder that the connection to the spectral function relies on the presence of an initial condensate. This explicitly shows how measuring the heating rate of the condensate due to trap modulation is equivalent to standard protocols for measuring polaron properties, such as radio-frequency spectroscopy [54,55].

APPENDIX E: BRAGG SPECTROSCOPY

In the case of Bragg spectroscopy, the time-dependent perturbation becomes

$$\hat{V}_\Omega(t) = \Omega \int d^3 r 2\cos(\mathbf{q}.\mathbf{r}_\perp + q_z z - \omega t)\hat{\psi}^\dagger(\mathbf{r})\hat{\psi}(\mathbf{r}), \tag{E1}$$

where Ω is proportional to the intensity of the applied field. Here, we take the Bragg beams to be tilted, such that the imparted momentum is both in and out of the plane, corresponding to $\mathbf{q}$ and q_z, respectively. Using Eq. (D3), we then obtain

$$\hat{V}_\Omega(t) = \Omega \sum_{\mathbf{k},n,m} (e^{-i\omega t} Q_{nm} \hat{c}^\dagger_{\mathbf{k}+\mathbf{q},m} \hat{c}_{\mathbf{k}n} + e^{i\omega t} Q^*_{nm} \hat{c}^\dagger_{\mathbf{k}n} \hat{c}_{\mathbf{k}+\mathbf{q},m}), \tag{E2}$$

where

$$\begin{aligned} Q_{nm} &\equiv \int_{-\infty}^{\infty} dz \varphi_n(z) e^{iq_z z} \varphi_m(z) \\ &= \delta_{nm}\left(1 - \frac{q_z^2 l_z^2}{4}(2n+1)\right) + i q_z l_z \left(\sqrt{\frac{n+1}{2}}\delta_{n+1,m} + \sqrt{\frac{n}{2}}\delta_{n-1,m}\right) \\ &\quad - \frac{q_z^2 l_z^2}{4}\left(\sqrt{(n+1)(n+2)}\delta_{n+2,m} + \sqrt{n(n-1)}\delta_{n-2,m}\right) + \cdots. \end{aligned} \tag{E3}$$

Now, the observable in the experiment is the rate of in-plane momentum transfer,

$$\frac{d\mathbf{P}}{dt} = -i\langle\psi|U^\dagger(t)[\hat{\mathbf{P}}, \hat{V}_\Omega(t)]U(t)|\psi\rangle, \tag{E4}$$

with the total in-plane momentum operator,

$$\hat{\mathbf{P}} = \sum_{\mathbf{k}n} \mathbf{k} \hat{c}^\dagger_{\mathbf{k}n} \hat{c}_{\mathbf{k}n}. \tag{E5}$$

Using the fact that $\hat{\mathbf{P}}$ is conserved in the unperturbed system, i.e., $[\hat{\mathbf{P}}, \hat{H}] = 0$, and

$$[\hat{\mathbf{P}}, \hat{V}_\Omega(t)] = \Omega\mathbf{q} \sum_{\mathbf{k},n,m} \left(Q_{nm} e^{-i\omega t} \hat{c}^\dagger_{\mathbf{k}+\mathbf{q},m} \hat{c}_{\mathbf{k}n} - \mathrm{H.c.}\right), \tag{E6}$$

and then expanding the time evolution operator $\hat{U}(t)$ as in Eq. (D9), we finally obtain

$$\frac{d\mathbf{P}}{dt} = \Omega^2 \mathbf{q} \int_{-\infty}^{t} dt' \sum_{\substack{\mathbf{k},\mathbf{k}' \\ n,n',m,m'}} \left\langle \left[\left(Q_{n'm'} e^{-i\omega t'} \hat{c}^\dagger_{\mathbf{k}'+\mathbf{q},m'}(t') \hat{c}_{\mathbf{k}n'}(t') + \mathrm{H.c.}\right), \left(Q_{nm} e^{-i\omega t} \hat{c}^\dagger_{\mathbf{k}+\mathbf{q},m}(t) \hat{c}_{\mathbf{k}n}(t) - \mathrm{H.c.}\right) \right] \right\rangle. \tag{E7}$$

Performing the same approximation as before, where we take $\hat{c}_{0,0}(t) \simeq \sqrt{n_0} e^{-i\mu_{\mathrm{B}} t}$, and then dropping terms that do not conserve momentum since these vanish due to translational symmetry, we have

$$\begin{aligned} \frac{d\mathbf{P}}{dt} &\simeq 2\Omega^2 n_0 \mathbf{q} \sum_n |Q_{n0}|^2 \left\{ \mathrm{Re}\left[\int_{-\infty}^{t} dt' e^{i(\mu_{\mathrm{B}}+\omega)(t-t')} \langle \hat{c}_{\mathbf{q}n}(t) \hat{c}^\dagger_{\mathbf{q}n}(t') \rangle\right] - \mathrm{Re}\left[\int_{-\infty}^{t} dt' e^{i(\mu_{\mathrm{B}}-\omega)(t-t')} \left\langle \hat{c}_{-\mathbf{q}n}(t) \hat{c}^\dagger_{-\mathbf{q}n}(t') \right\rangle\right] \right\} \\ &= 2\Omega^2 n_0 \mathbf{q} \sum_n |Q_{n0}|^2 \left\{ \mathrm{Re}\left[\int_{0}^{\infty} dt' e^{i(\mu_{\mathrm{B}}+\omega)t} \langle \hat{c}_{\mathbf{q}n}(t) \hat{c}^\dagger_{\mathbf{q}n}(0) \rangle\right] - \mathrm{Re}\left[\int_{0}^{\infty} dt' e^{i(\mu_{\mathrm{B}}-\omega)t} \left\langle \hat{c}_{-\mathbf{q}n}(t) \hat{c}^\dagger_{-\mathbf{q}n}(0) \right\rangle\right] \right\} \\ &= -2\Omega^2 n_0 \mathbf{q} \sum_n |Q_{n0}|^2 \{\operatorname{Im} G_n(\mathbf{q}, \mu_{\mathrm{B}} + \omega) - \operatorname{Im} G_n(-\mathbf{q}, \mu_{\mathrm{B}} - \omega)\}, \end{aligned} \tag{E8}$$

where $G_n(\mathbf{q},\omega)$ corresponds to the retarded Green's function for an impurity with in-plane momentum $\mathbf{q}$ and harmonic oscillator quantum number (or synthetic spin) n. Like before, we can drop the second term for large frequencies $\omega > \omega_z$ since it is off resonant and corresponds to removing energy from the system rather than adding energy.

Finally, if the response for different quantum numbers n is spectrally separated, like it is in experiment, we can select out different components by tuning the frequency to be near resonant with $n\omega_z$ and dropping off-resonant terms. Then we once again find that the response is proportional to the impurity spectral function:

$$\frac{d\mathbf{P}}{dt} \propto n_0 \mathbf{q} |Q_{n0}|^2 A_n(\mathbf{q}, \mu_B + \omega). \tag{E9}$$

This time, the spectrum is momentum resolved, allowing us to access the effective mass of the polaron. Note that the coupling to the $n \neq 0$ modes vanishes if the out-of-plane component $q_z \to 0$; thus, any measurement of the polaron effective mass requires the Bragg beams to be tilted.

1. Tilted Bragg in the experiment

In the experiment, Bragg spectroscopy is implemented by focusing two parallel beams far from resonance at $\lambda = 780$ nm onto the atoms by using a high NA microscope. The angle that controls the momentum transfer q can be set by changing the distance between the beams before the microscope. Additionally, each beam has an individual acousto-optic modulator to introduce a frequency difference ω_m between the beams, leading to an energy transfer of $\hbar\omega_m$. For excitation into the $n_z = 1$ and $n_z = 2$ states, an out-of-plane momentum q_z is introduced by slightly misplacing the center of the beams by $\sim$1 mm from the center of the microscope, such that q_z has only $\sim$5% of the total momentum. Using Eq. (E3), we can compare the coupling within the ground state to the coupling of the $n_z = 1$ and $n_z = 2$ impurity states:

$$\begin{aligned} |Q_{00}|^2 &= \left(1 - \frac{q_z^2 l_z^2}{4}\right)^2, \\ |Q_{10}|^2 &= \frac{q_z^2 l_z^2}{2}, \\ |Q_{20}|^2 &= \frac{q_z^4 l_z^4}{8}. \end{aligned} \tag{E10}$$

APPENDIX F: *T*-MATRIX DESCRIPTION OF THE POLARON QUASIPARTICLE

1. Interactions in the quasi-2D system

Let us start by considering the interaction term $\hat{U}_{\text{int}}$ in the quasi-2D Hamiltonian in Eq. (D6), which is the standard boson-boson interaction in 3D:

$$\hat{U}_{\text{int}} = \frac{1}{2}\int d^3r \int d^3r' V(\mathbf{r}-\mathbf{r}')\hat{\psi}^\dagger(\mathbf{r})\hat{\psi}^\dagger(\mathbf{r}')\hat{\psi}(\mathbf{r}')\hat{\psi}(\mathbf{r}), \tag{F1}$$

where $V(\mathbf{r})$ is the interaction potential between bosons. Using Eq. (D3) to write it in the harmonic oscillator (HO) basis gives

$$\hat{U}_{\text{int}} = \frac{1}{2}\sum_{\mathbf{k},\mathbf{k}',\mathbf{q}} \sum_{\substack{n_1,n_2 \\ n_3,n_4}} V^{n_1 n_2}_{n_3 n_4} \hat{c}^\dagger_{\mathbf{k},n_1} \hat{c}^\dagger_{\mathbf{k}',n_2} \hat{c}_{\mathbf{k}'+\mathbf{q},n_3} \hat{c}_{\mathbf{k}'-\mathbf{q},n_4}, \tag{F2}$$

where

$$V^{n_1 n_2}_{n_3 n_4} = g\sqrt{2\pi} l_z \sum_{N\nu\nu'} f_\nu \langle n_1 n_2 | N\nu\rangle f_{\nu'} \langle N\nu' | n_3 n_4\rangle, \tag{F3}$$

and we have assumed short-range interactions with strength g. Here $\langle n_1 n_2 | N\nu\rangle$ is the (real) Clebsch-Gordan coefficient to go from the HO motion of two particles in the n_1 and n_2 levels to the center-of-mass and relative motion quantum numbers N and ν, respectively [56]. This is zero unless $n_1 + n_2 = N + \nu$. Also, the coefficients f_ν are only nonzero if ν is even and they correspond to the HO wave function of the relative motion at zero separation:

$$|f_\nu|^2 = \frac{1}{\sqrt{2\pi} l_z} \frac{(\nu-1)!!}{\nu!!}. \tag{F4}$$

To understand the role of exchange in the impurity-medium interactions, consider the simple noninteracting state involving an $n = 0$ condensate of density n_0 and a single boson in the $n \neq 0$ level:

$$|\Psi\rangle = \hat{c}^\dagger_{0,n} |\text{BEC}_0\rangle. \tag{F5}$$

This is the starting state for any polaron theory. Then we have the expectation value:

$$\langle\Psi|\hat{U}_{\text{int}}|\Psi\rangle = \frac{1}{2} n_0 [V^{0n}_{0n} + V^{n0}_{0n} + V^{0n}_{n0} + V^{n0}_{n0}] = 2 n_0 V^{0n}_{0n}, \tag{F6}$$

since the ordering of indices in $V^{n_1 n_2}_{n_3 n_4}$ does not change the coefficient. Thus, we automatically arrive at a factor of 2 due to the exchange of bosons. Note that we can get something different from a factor of 2 if the ordering of indices does change the interaction coefficient, which would happen if the range of the potential is important.

Note that the factor of 2 appearing in Eq. (F6) is different from that expected in the clock shift of a thermal Bose gas [47]. Specifically, this factor of 2 is a feature of scattering which occurs regardless of how we drive a transition from one internal state to another. For instance, exchange processes also occur in the scattering of otherwise identical atoms in different hyperfine states. However, in practice this is hidden in the microscopic details of the atom-atom interactions that underlie the effective low-energy scattering parameters.

2. General formalism for spectroscopy

The Green's function for an impurity particle (i.e., a particle that has been removed from the condensate) satisfies the Dyson equation,

$$G_{nm}(\mathbf{k},\omega) = \left[G^{(0)}_{nm}(\mathbf{k},\omega)^{-1} - \Sigma_{nm}(\mathbf{k},\omega)\right]^{-1}. \tag{F7}$$

n and m are the incoming and outgoing harmonic oscillator indices of the transverse motion. In the absence of interactions, this index is preserved and we have

$$G^{(0)}_{nm}(\mathbf{k},\omega) = \frac{\delta_{nm}}{\omega - n\omega_z - \epsilon_{\mathbf{k}}} \equiv G^{(0)}_{n}(\mathbf{k},\omega)\delta_{nm}. \tag{F8}$$

$\epsilon_{\mathbf{k}} = k^2/2m$ is the bare impurity dispersion. The question is which approximations we should apply to arrive at the self-energy Σ, and thus the spectral function.

Assuming that the response is dominated by two-body correlations, the self-energy due to an impurity interacting with a condensate in the ground state is (see Ref. [57])

$$\Sigma_{nm}(\mathbf{k},\omega) = 2n_0 T^{n0}_{m0}(\mathbf{k},\omega), \tag{F9}$$

where the factor 2 arises from exchange, as discussed above. Here, T^{m0}_{n0} is the T matrix for an incoming or outgoing pair of particles with HO indices $\{n,0\}$ and $\{m,0\}$.

According to Refs. [53,57,58], we go into the c.m. frame (scattering is independent of the c.m. motion) via

$$T^{m0}_{n0}(\mathbf{k},\omega) = \sum_{N,\nu,\nu'} \sqrt{2\pi}\, l_z f_\nu f_{\nu'} \langle n0|N\nu\rangle \mathcal{T}(\omega - N\omega_z - \epsilon_{\mathbf{k}}/2)\langle N\nu'|m0\rangle. \tag{F10}$$

Here, $\mathcal{T}$ is the effective quasi-2D dimer-dimer scattering T matrix at collision energy E:

$$\mathcal{T}(E) = \frac{\sqrt{8\pi}}{m}\frac{1}{\frac{l_z}{a_{3D}} - \mathcal{F}(-E/\omega_z)}, \tag{F11}$$

where $l_z = \sqrt{\hbar/m\omega_z}$ is the harmonic oscillator length and [52]

$$\mathcal{F}(x) = \int_0^\infty \frac{du}{\sqrt{4\pi u^3}}\left[1 - \frac{e^{-xu}}{\sqrt{[1-e^{-2u}]/2u}}\right]. \tag{F12}$$

At low energies compared to the transverse confinement, the function $\mathcal{F}$ takes the form $\mathcal{F}(x) \simeq \ln(\pi x/B)/\sqrt{2\pi}$, with $B \approx 0.905$. This is consistent with the universal low-energy form of the 2D scattering amplitude in Eq. (B2).

3. Approximating the number of involved levels

In Bragg spectroscopy, we measure the spectral functions A_1 and A_2, while in trap modulation spectroscopy we measure A_2. Furthermore, the frequency is always close to either ω_z or $2\omega_z$. It is therefore reasonable to consider the approximations

$$G_1(\mathbf{k},\omega) \equiv G_{11}(\mathbf{k},\omega) \simeq \frac{1}{\omega - \epsilon_{\mathbf{k}} - \omega_z - \Sigma_{11}(\mathbf{k},\omega)}, \tag{F13}$$

$$G_2(\mathbf{k},\omega) \equiv G_{22}(\mathbf{k},\omega) \simeq \frac{1}{\omega - \epsilon_{\mathbf{k}} - 2\omega_z - \Sigma_{22}(\mathbf{k},\omega)}. \tag{F14}$$

We have checked that this approximation works extremely well for the results presented in this work.

4. Impurity self-energy

a. $n = 2$

For the $n = 2$ impurity, we are interested in $\Sigma_{22}(\mathbf{k},\omega) = 2n_0 T^{20}_{20}(\mathbf{k},\omega)$, in which case there are two nonvanishing Clebsch-Gordan coefficients that allow one to go from individual particles with harmonic oscillator indices 0 and 2 into the c.m. frame:

$$\langle N=2,\nu=0|n_1=0,n_2=2\rangle = \langle N=0,\nu=2|n_1=0,n_2=2\rangle = 1/2. \tag{F15}$$

Furthermore, we have

$$\sqrt{2\pi} l_z f_0^2 = 1, \qquad \sqrt{2\pi} l_z f_2^2 = 1/2. \tag{F16}$$

Putting everything together using Eqs. (F9) and (F10), we find

$$\Sigma_{22}(\mathbf{k},\omega) = 2n_0\left[\frac{1}{8}\frac{\sqrt{2\pi}}{m_r}\frac{1}{\frac{l_z}{a_s} - \mathcal{F}(-\omega/\omega_z + \epsilon_{\mathbf{k}}/2\omega_z)} + \frac{1}{4}\frac{\sqrt{2\pi}}{m_r}\frac{1}{\frac{l_z}{a_s} - \mathcal{F}(-\omega/\omega_z + 2 + \epsilon_{\mathbf{k}}/2\omega_z)}\right]. \tag{F17}$$

The nontrivial energy dependence in $\mathcal{F}$ is due to the fact that the harmonic oscillator energy of the two scattering particles can go into either the relative or the c.m. motion, while the collision energy depends only on the relative motion. In the strongly interacting regime, the first term—where the total harmonic oscillator energy of $2\omega_z$ goes into the relative motion—primarily leads to a broadening. The origin of this broadening is decay due to coupling of the high-energy transverse motion with high-momentum states in the lowest level of the transverse motion, a decay process that would also be present for a truly distinguishable impurity in the $n = 2$ level. On the other hand, the second term where the harmonic oscillator energy goes into the center-of-mass motion features no such decay process and is responsible for most of the quasiparticle energy shift. In practice, we find that there is an approximate cancellation between the effects of exchange and decay, thus explaining the excellent agreement with QMC.

In the limit of weak interactions, $l_z/a_s \gg 1$, this reduces to

$$\Sigma_{22}(\mathbf{k},\omega) = 2n_0 \frac{3}{8}\frac{\sqrt{2\pi}a_s}{m_r l_z} \equiv E_{\mathrm{MF},2}. \tag{F18}$$

This is independent of the energy itself, and corresponds to the mean-field energy shift $E_{\mathrm{MF},2}$. We can also arrive at this expression by taking an effective quasi-2D interaction constant:

$$\frac{2\pi a_s}{m_r}\int dz |\varphi_0(z)|^2 |\varphi_2(z)|^2 = \frac{3}{8}\frac{\sqrt{2\pi}a_s}{m_r l_z}. \tag{F19}$$

b. $n = 1$

For the $n = 1$ impurity, we instead have

$$\Sigma_{11}(\mathbf{k},\omega) = 2n_0 \frac{1}{2}\frac{\sqrt{2\pi}}{m_r}\frac{1}{\frac{l_z}{a_s} - \mathcal{F}(-\omega/\omega_z + 1 + \epsilon_{\mathbf{k}}/2\omega_z)}, \tag{F20}$$

where we again use Eqs. (F9) and (F10). The associated mean-field energy shift is

$$E_{\mathrm{MF},1} = n_0 \frac{\sqrt{2\pi}a_s}{m_r l_z}. \tag{F21}$$

Note that, unlike the $n = 2$ case above, the total transverse motion of $n = 1$ can only go into the center of mass, and therefore there are no decay channels associated with the transverse relative motion. Indeed, Fig. 4(c) shows that the $n = 1$ spectrum remains exceptionally narrow across all momenta probed.

Remarkably, the self-energy for the $n = 1$ level appears as though the impurity-medium interactions are precisely those between two medium particles due to a cancellation between the factor 2 from exchange and a factor $1/2$ from the Clebsch-Gordan coefficient:

$$\langle N = 1, \nu = 0 | n_1 = 0, n_2 = 1\rangle = 1/2. \tag{F22}$$

Therefore, we expect no interaction-induced energy shift at zero momentum. This is precisely what is observed in our experiment.

5. Approximating repulsive interactions

Since the quasi-2D resummation of the interactions in Refs. [30,52] applies to attractive interactions, we need some modifications to better represent true repulsive interactions. In particular, we note that for a repulsive interaction we always evaluate the self-energy at a shifted energy; i.e., we take $\Sigma(\omega) \to \Sigma(\omega - E_{\mathrm{MF}})$, with E_{MF} the mean-field energy for either $n = 1$ or $n = 2$. This ensures that the repulsive branch is shifted up, as it should be for a true repulsive interaction, and it is consistent with variational approaches to repulsive interactions [7].

We therefore find the impurity spectral functions:

$$A_1(\mathbf{k},\omega) = -\frac{1}{\pi}\mathrm{Im}\frac{1}{\omega - \omega_z - \epsilon_{\mathbf{k}} - \Sigma_{11}(\mathbf{k},\omega - E_{\mathrm{MF},1})}, \tag{F23}$$

$$A_2(\mathbf{k},\omega) = -\frac{1}{\pi}\mathrm{Im}\frac{1}{\omega - 2\omega_z - \epsilon_{\mathbf{k}} - \Sigma_{22}(\mathbf{k},\omega - E_{\mathrm{MF},2})}. \tag{F24}$$

These are then used to extract the polaron energies, effective masses, and residues shown in the main text. Note that when comparing with Δ, we use μ_{B} extracted from the QMC calculations; see below.

APPENDIX G: MONTE CARLO SIMULATION DETAILS

The quantum Monte Carlo algorithm is well suited for computing the ground-state energy of bosonic systems. It can also be extended to evaluate the energy of specific excited states, provided their nodal structure is known. Below, we summarize the key modifications required to treat the $n = 1$ and $n = 2$ excitations.

We model dimers as a system of N hard spheres with diameter equal to the three-dimensional s-wave dimer-dimer scattering length $a_{3\mathrm{D}}$ and mass m, corresponding to the mass of a dimer. In this way, the bosonic model Hamiltonian provides a fully three-dimensional description, treating dimers as structureless bosons, trapped in the transverse confinement,

$$\hat{H} = -\frac{\hbar^2}{2m}\sum_{i=1}^{N}\left(\frac{\partial^2}{\partial x_i^2} + \frac{\partial^2}{\partial y_i^2} + \frac{\partial^2}{\partial z_i^2}\right) + \frac{m\omega_z^2}{2}\sum_{i=1}^{N} z_i^2 + \sum_{i<j}^{N} V_{\mathrm{HS}}(|\mathbf{r}_i - \mathbf{r}_j|), \tag{G1}$$

where the hard-sphere (HS) interaction potential is defined as

$$V_{\mathrm{HS}}(r) = \begin{cases} +\infty & r < a_{3\mathrm{D}} \\ 0 & r \geq a_{3\mathrm{D}}. \end{cases} \tag{G2}$$

We consider a ground-state guiding wave function of the form

$$\Psi_0(\mathbf{r}_1, \ldots, \mathbf{r}_N) = \prod_{i=1}^{N} f_1(\mathbf{r}_i) \prod_{i<j} f_2(|\mathbf{r}_i - \mathbf{r}_j|), \tag{G3}$$

where $\mathbf{r} = (x, y, z)$ and the one-body term $f_1(\mathbf{r})$ accounts for the external harmonic confinement along the z direction,

$$f_1(\mathbf{r}) = \exp(-\alpha z^2/l_z^2), \tag{G4}$$

with α being a variational parameter whose value is optimized by minimizing the variational energy. For small values of the gas parameter, $\alpha = 1/2$ corresponds to the single-particle ground state of a harmonic oscillator, $f_1(z) = H_0(z)$. The two-body Jastrow term $f_2(r)$ is constructed by matching the short-range two-body scattering problem at short distances to long-range phononic asymptotics.

To describe an excited state, we multiply the nodeless ground-state wave function Ψ_0 by a nodal N-body term f_N:

$$\Psi(\mathbf{r}_1, \ldots, \mathbf{r}_N) = \Psi_0(\mathbf{r}_1, \ldots, \mathbf{r}_N) f_N(\mathbf{r}_1, \ldots, \mathbf{r}_N). \tag{G5}$$

The drift force acting on particle i gets an additional N-body contribution:

$$\mathbf{F}_i = \frac{\nabla_i \Psi}{\Psi} = \frac{\nabla_i \Psi_0}{\Psi_0} + \frac{\nabla_i f_N}{f_N} = \mathbf{F}_i^{(0)} + \mathbf{F}_i^{(N)}. \tag{G6}$$

Also, the contribution of particle i to the kinetic energy has additional terms:

$$\begin{aligned} T_i &= -\frac{\hbar^2}{2m} \frac{\Delta_i \Psi}{\Psi} \\ &= -\frac{\hbar^2}{2m} \left[\frac{\Delta_i \Psi_0}{\Psi_0} + 2 \frac{\nabla_i \Psi_0}{\Psi_0} \cdot \frac{\nabla_i f_N}{f_N} + \frac{\Delta_i f_N}{f_N} \right]. \end{aligned}$$

Summing over all particles, the total kinetic energy reads

$$T = T_0 - 2\frac{\hbar^2}{2m} \sum_i \mathbf{F}_i^{(0)} \cdot \mathbf{F}_i^{(N)} - \frac{\hbar^2}{2m} \sum_i \frac{\Delta_i f_N}{f_N}, \tag{G7}$$

where T_0 is the contribution to the kinetic energy calculated with respect to the ground-state wave function.

For an $n = 1$ excitation, particle i can occupy the first excited harmonic oscillator state, $H_1(z_i) \sim z_i \exp(-z_i^2/2)$, which corresponds to multiplying Ψ_0 by z_i. Symmetrizing over all particles leads to the following choice,

$$f_N(\mathbf{r}_1, \ldots, \mathbf{r}_N) = \sum_{i=1}^{N} (z_i - \langle z \rangle), \tag{G8}$$

which introduces a single node when the center-of-mass coordinate $z_{\mathrm{c.m.}} = \sum_i z_i/N$ coincides with its average position, which in the considered case corresponds to the center of the trap, $\langle z \rangle = 0$. The excitation contribution to the drift force is

$$\mathbf{F}_i^{(N)} = \frac{\nabla_i f_N}{f_N} = \frac{1}{f_N} \hat{z}, \tag{G9}$$

which diverges when $f_N = 0$, i.e., at $z_{\mathrm{c.m.}} = 0$. This divergence ensures that such configurations are not sampled during the Monte Carlo simulation. In contrast, the second derivatives vanish, $\Delta_i f_N = 0$, and thus the last term in Eq. (G7) drops out for $n = 1$ excitation. The only contribution comes from the product of drift forces, in which the drift force Eq. (G6) describing the excitation has elements only along z and all of them are equal to $1/f_N$, so that for $n = 1$,

$$T = T_0 - 2\frac{\hbar^2}{2m} \sum_i \frac{F_{i,z}^{(0)}}{f_N}. \tag{G10}$$

For an $n = 2$ excitation, particle i can occupy the second excited harmonic oscillator state, $H_2(z_i) \sim (z_i^2 - 1/2) \times \exp(-z_i^2/2)$, which corresponds to multiplying Ψ_0 by $(z_i^2 - 1/2)$ (here we use dimensionless notation corresponding to the harmonic oscillator units). We consider the following symmetrized N-body term,

$$f_N(\mathbf{r}_1, \ldots, \mathbf{r}_N) = \sum_{i=1}^{N} (z_i^2 - \langle z^2 \rangle), \tag{G11}$$

where the sum corresponds to the instantaneous average value of mean square dispersion and we subtract its average value. This wave function has two nodes.

The excitation contribution to the drift force is

$$\mathbf{F}_i^{(N)} = \frac{2z_i}{f_N} \hat{z}, \tag{G12}$$

and to the kinetic energy is

$$T = T_0 - 2\frac{\hbar^2}{m} \sum_{i=1}^{N} \frac{F_{i,z}^{(0)} z_i}{f_N} - \frac{\hbar^2}{m} \frac{N}{f_N}. \tag{G13}$$

The first odd excitation ($n = 1$) imposes a node in the center-of-mass coordinate at $z_{\mathrm{c.m.}} = 0$, which, on average, corresponds to the central position of the trap, $\mathbf{z} = \langle z_{\mathrm{c.m.}} \rangle = 0$. This location of the node is natural, as the wave function of the first excited state must be orthogonal to the ground state.

The resulting density profiles for the $n = 0$ and $n = 1$ states are symmetric with respect to $z = 0$, while the wave function for $n = 1$ is antisymmetric. This property holds for any interaction strength and allows one to carry out QMC simulations of the $n = 1$ state. In contrast, the nodal surface imposed for the $n = 2$ state assumes that the ground-state density corresponds to that of a noninteracting Bose gas, which is valid in the weakly interacting regime.

To verify that the proposed many-body wave functions correctly describe the $n = 1$ and $n = 2$ excitations, we test them on one-dimensional ideal gases confined in a harmonic trap—namely, the ideal Bose gas with $f_1(z) = \exp(-z^2/2)$ and $f_2(z) = 1$, and the ideal Fermi gas with the same $f_1(z)$ and $f_2(z) = z$. It can be explicitly verified that the ground-state wave function Eq. (G3) and the first two excited states Eq. (G5) are exact for any number of particles, taking into account that $\langle z^2 \rangle = 1/2$ for ideal bosons and $\langle z^2 \rangle = N/2$ for ideal fermions. The corresponding excitation energies are $\hbar\omega$ and $2\hbar\omega$ for the $n = 1$ and $n = 2$ excitations, respectively. As we are interested in the quasi-two-dimensional regime, where the density profile is similar to the Gaussian profile of the ideal Bose gas, in the calculations we assume $\langle z^2 \rangle = 1/2$.

For the excitation with a finite momentum, we consider a different symmetric many-body term that introduces a node in the x component of the center-of-mass coordinate. Specifically, we multiply the nodeless wave function by

$$f_N(\mathbf{r}_1, \ldots, \mathbf{r}_N) = \cos(k_\ell x_{\mathrm{c.m.}}), \tag{G14}$$

where $k_\ell = \pi\ell/L$ with $\ell = 0; \pm 1; \pm 2; \ldots$ defines the excitation momentum and $x_{\mathrm{c.m.}} = (1/N)\sum_{i=1}^{N} x_i$ is the c.m. coordinate along the in-plane (x) direction.

The gradient with respect to particle i is

$$\nabla_i f_N = \frac{\partial f_N}{\partial x_i}\hat{x} = -\frac{k_\ell}{N}\sin(k_\ell x_{\mathrm{c.m.}})\hat{x}, \tag{G15}$$

so the drift force contribution becomes

$$\mathbf{F}_i^{(N)} = \frac{\nabla_i f_N}{f_N} = -\frac{k_\ell}{N}\tan(k_\ell x_{\mathrm{c.m.}})\hat{x}. \tag{G16}$$

The Laplacian of f_N with respect to x_i is

$$\Delta_i f_N = \frac{\partial^2 f_N}{\partial x_i^2} = -\left(\frac{k_\ell}{N}\right)^2 \cos(k_\ell x_{\mathrm{c.m.}}), \tag{G17}$$

and dividing by f_N, we obtain

$$\frac{\Delta_i f_N}{f_N} = -\left(\frac{k_\ell}{N}\right)^2. \tag{G18}$$

Summing over all particles, the total additional contribution to the kinetic energy is

$$T = T_0 + \frac{\hbar^2 k_\ell}{Nm}\sum_{i=1}^{N} F_{xi}^{(0)} \tan(k_\ell x_{\mathrm{c.m.}}) + \frac{\hbar^2}{2Nm}k_\ell^2. \tag{G19}$$

The contribution from only the last term corresponds to a center-of-mass excitation with an effective mass $m^* = Nm$.

[1] L. D. Landau and S. I. Pekar, *Effective mass of a polaron*, Zh. Eksp. Teor. Fiz. **18**, 419 (1948).

[2] J. Bardeen, G. Baym, and D. Pines, *Effective interaction of* ^{3}He *atoms in dilute solutions of* ^{3}He *in* ^{4}He *at low temperatures*, Phys. Rev. **156**, 207 (1967).

[3] M. Sidler, P. Back, O. Cotlet, A. Srivastava, T. Fink, M. Kroner, E. Demler, and A. Imamoglu, *Fermi polaron-polaritons in charge-tunable atomically thin semiconductors*, Nat. Phys. **13**, 255 (2017).

[4] P. A. Lee, N. Nagaosa, and X.-G. Wen, *Doping a Mott insulator: Physics of high-temperature superconductivity*, Rev. Mod. Phys. **78**, 17 (2006).

[5] C. Chin, R. Grimm, P. Julienne, and E. Tiesinga, *Feshbach resonances in ultracold gases*, Rev. Mod. Phys. **82**, 1225 (2010).

[6] P. Massignan, M. Zaccanti, and G. M. Bruun, *Polarons, dressed molecules and itinerant ferromagnetism in ultracold Fermi gases*, Rep. Prog. Phys. **77**, 034401 (2014).

[7] F. Scazza, M. Zaccanti, P. Massignan, M. M. Parish, and J. Levinsen, *Repulsive Fermi and Bose polarons in quantum gases*, Atoms **10**, 55 (2022).

[8] A. Schirotzek, C.-H. Wu, A. Sommer, and M. W. Zwierlein, *Observation of Fermi polarons in a tunable Fermi liquid of ultracold atoms*, Phys. Rev. Lett. **102**, 230402 (2009).

[9] M. Koschorreck, D. Pertot, E. Vogt, B. Fröhlich, M. Feld, and M. Köhl, *Attractive and repulsive Fermi polarons in two dimensions*, Nature (London) **485**, 619 (2012).

[10] M.-G. Hu, M. J. Van de Graaff, D. Kedar, J. P. Corson, E. A. Cornell, and D. S. Jin, *Bose polarons in the strongly interacting regime*, Phys. Rev. Lett. **117**, 055301 (2016).

[11] N. B. Jørgensen, L. Wacker, K. T. Skalmstang, M. M. Parish, J. Levinsen, R. S. Christensen, G. M. Bruun, and J. J. Arlt, *Observation of attractive and repulsive polarons in a Bose-Einstein condensate*, Phys. Rev. Lett. **117**, 055302 (2016).

[12] N. Darkwah Oppong, L. Riegger, O. Bettermann, M. Höfer, J. Levinsen, M. M. Parish, I. Bloch, and S. Fölling, *Observation of coherent multiorbital polarons in a two-dimensional Fermi gas*, Phys. Rev. Lett. **122**, 193604 (2019).

[13] Z. Z. Yan, Y. Ni, C. Robens, and M. W. Zwierlein, *Bose polarons near quantum criticality*, Science **368**, 190 (2020).

[14] J. Etrych, G. Martirosyan, A. Cao, C. J. Ho, Z. Hadzibabic, and C. Eigen, *Universal quantum dynamics of Bose polarons*, Phys. Rev. X **15**, 021070 (2025).

[15] C. Kohstall, M. Zaccanti, M. Jag, A. Trenkwalder, P. Massignan, G. M. Bruun, F. Schreck, and R. Grimm, *Metastability and coherence of repulsive polarons in a strongly interacting Fermi mixture*, Nature (London) **485**, 615 (2012).

[16] F. Scazza, G. Valtolina, P. Massignan, A. Recati, A. Amico, A. Burchianti, C. Fort, M. Inguscio, M. Zaccanti, and G. Roati, *Repulsive Fermi polarons in a resonant mixture of ultracold ^{6}Li atoms*, Phys. Rev. Lett. **118**, 083602 (2017).
[17] A. M. Morgen, S. S. Balling, K. K. Nielsen, T. Pohl, G. M. Bruun, and J. J. Arlt, *Quantum beat spectroscopy of repulsive Bose polarons*, Phys. Rev. Res. **7**, L022002 (2025).
[18] J. Levinsen, M. M. Parish, and G. M. Bruun, *Impurity in a Bose-Einstein condensate and the Efimov effect*, Phys. Rev. Lett. **115**, 125302 (2015).
[19] P. Naidon and S. Endo, *Efimov physics: A review*, Rep. Prog. Phys. **80**, 056001 (2017).
[20] F. Grusdt and M. Fleischhauer, *Tunable polarons of slow-light polaritons in a two-dimensional Bose-Einstein condensate*, Phys. Rev. Lett. **116**, 053602 (2016).
[21] V. Pastukhov, *Polaron in dilute 2D Bose gas at low temperatures*, J. Phys. B **51**, 155203 (2018).
[22] L. A. Peña Ardila, G. E. Astrakharchik, and S. Giorgini, *Strong coupling Bose polarons in a two-dimensional gas*, Phys. Rev. Res. **2**, 023405 (2020).
[23] H. Tajima, J. Takahashi, S. I. Mistakidis, E. Nakano, and K. Iida, *Polaron problems in ultracold atoms: Role of a Fermi sea across different spatial dimensions and quantum fluctuations of a Bose medium*, Atoms **9**, 18 (2021).
[24] L. F. Cárdenas-Castillo and A. Camacho-Guardian, *Strongly interacting Bose polarons in two-dimensional atomic gases and quantum fluids of polaritons*, Atoms **11**, 3 (2023).
[25] Y. Nakano, M. M. Parish, and J. Levinsen, *Variational approach to the two-dimensional Bose polaron*, Phys. Rev. A **109**, 013325 (2024).
[26] W. Zwerger, *The BCS-BEC Crossover and the Unitary Fermi Gas* (Springer Science & Business Media, New York, 2011), Vol. 836.
[27] D. S. Petrov, C. Salomon, and G. V. Shlyapnikov, *Weakly bound dimers of fermionic atoms*, Phys. Rev. Lett. **93**, 090404 (2004).
[28] K. Hueck, N. Luick, L. Sobirey, J. Siegl, T. Lompe, and H. Moritz, *Two-dimensional homogeneous Fermi gases*, Phys. Rev. Lett. **120**, 060402 (2018).
[29] L. Sobirey, N. Luick, M. Bohlen, H. Biss, H. Moritz, and T. Lompe, *Observation of superfluidity in a strongly correlated two-dimensional Fermi gas*, Science **372**, 844 (2021).
[30] D. S. Petrov and G. V. Shlyapnikov, *Interatomic collisions in a tightly confined Bose gas*, Phys. Rev. A **64**, 012706 (2001).
[31] C. R. Cabrera, R. Henke, L. Broers, J. Skulte, H. P. Ojeda Collado, H. Biss, L. Mathey, and H. Moritz, *Hybridization of the amplitude mode in a confined fermionic superfluid*, Phys. Rev. Res. **7**, L032018 (2025).
[32] R. Scelle, T. Rentrop, A. Trautmann, T. Schuster, and M. K. Oberthaler, *Motional coherence of fermions immersed in a Bose gas*, Phys. Rev. Lett. **111**, 070401 (2013).
[33] T. Rentrop, A. Trautmann, F. A. Olivares, F. Jendrzejewski, A. Komnik, and M. K. Oberthaler, *Observation of the phononic Lamb shift with a synthetic vacuum*, Phys. Rev. X **6**, 041041 (2016).
[34] M. Schick, *Two-dimensional system of hard-core bosons*, Phys. Rev. A **3**, 1067 (1971).
[35] G. E. Astrakharchik, J. Boronat, J. Casulleras, I. L. Kurbakov, and Y. E. Lozovik, *Equation of state of a weakly interacting two-dimensional Bose gas studied at zero temperature by means of quantum Monte Carlo methods*, Phys. Rev. A **79**, 051602(R) (2009).
[36] Z. Hadzibabic and J. Dalibard, *Two-dimensional Bose fluids: An atomic physics perspective*, Riv. Nuovo Cimento **34**, 389 (2011).
[37] E. P. Bernard and W. Krauth, *Two-step melting in two dimensions: First-order liquid-hexatic transition*, Phys. Rev. Lett. **107**, 155704 (2011).
[38] F. Scazza, G. Valtolina, A. Amico, P. E. S. Tavares, M. Inguscio, W. Ketterle, G. Roati, and M. Zaccanti, *Exploring emergent heterogeneous phases in strongly repulsive Fermi gases*, Phys. Rev. A **101**, 013603 (2020).
[39] D. S. Petrov, C. Salomon, and G. V. Shlyapnikov, *Scattering properties of weakly bound dimers of fermionic atoms*, Phys. Rev. A **71**, 012708 (2005).
[40] L. A. Peña Ardila and S. Giorgini, *Impurity in a Bose-Einstein condensate: Study of the attractive and repulsive branch using quantum Monte Carlo methods*, Phys. Rev. A **92**, 033612 (2015).
[41] R. Schmidt and T. Enss, *Self-stabilized Bose polarons*, SciPost Phys. **13**, 054 (2022).
[42] H. Biss, L. Sobirey, N. Luick, M. Bohlen, J. J. Kinnunen, G. M. Bruun, T. Lompe, and H. Moritz, *Excitation spectrum and superfluid gap of an ultracold Fermi gas*, Phys. Rev. Lett. **128**, 100401 (2022).
[43] D. J. Wineland and W. M. Itano, *Laser cooling of atoms*, Phys. Rev. A **20**, 1521 (1979).
[44] For extraction of the curvature, we do not include the value at $q = 0$ from trap modulation spectroscopy, since there is a small systematic energy shift between both measurements.
[45] S. Nascimbène, N. Navon, K. J. Jiang, L. Tarruell, M. Teichmann, J. McKeever, F. Chevy, and C. Salomon, *Collective oscillations of an imbalanced Fermi gas: Axial compression modes and polaron effective mass*, Phys. Rev. Lett. **103**, 170402 (2009).
[46] Z. Yan, P. B. Patel, B. Mukherjee, R. J. Fletcher, J. Struck, and M. W. Zwierlein, *Boiling a unitary Fermi liquid*, Phys. Rev. Lett. **122**, 093401 (2019).
[47] D. M. Harber, H. J. Lewandowski, J. M. McGuirk, and E. A. Cornell, *Effect of cold collisions on spin coherence and resonance shifts in a magnetically trapped ultracold gas*, Phys. Rev. A **66**, 053616 (2002).
[48] J. Etrych, S. J. Morris, S. M. Fischer, G. Martirosyan, C. J. Ho, M. Drescher, M. Salmhofer, Z. Hadzibabic, T. Enss, and C. Eigen, *Fate of an impurity strongly interacting with a thermal Bose gas*, Phys. Rev. Lett. **137**, 193405 (2026).
[49] K. Gubbels and H. Stoof, *Imbalanced Fermi gases at unitarity*, Phys. Rep. **525**, 255 (2013).
[50] R. Henke, J. Levinsen, M. M. Parish, J. Boronat, G. E. Astrakharchik, H. Moritz, and C. R. Cabrera, *Realization of Repulsive Polarons in the Strongly Correlated Regime*, Version v2, 10.5281/zenodo.22960564 (2026).
[51] A. Deltuva, *Universality in fermionic dimer-dimer scattering*, Phys. Rev. A **96**, 022701 (2017).
[52] I. Bloch, J. Dalibard, and W. Zwerger, *Many-body physics with ultracold gases*, Rev. Mod. Phys. **80**, 885 (2008).
[53] J. Levinsen and M. M. Parish, *Strongly interacting two-dimensional Fermi gases*, in *Annual Review of Cold Atoms*

and Molecules (World Scientific, Singapore, 2015), Vol. 3, pp. 1–75.

[54] M. Punk and W. Zwerger, *Theory of rf-spectroscopy of strongly interacting fermions*, Phys. Rev. Lett. **99**, 170404 (2007).

[55] W. E. Liu, Z.-Y. Shi, M. M. Parish, and J. Levinsen, *Theory of radio-frequency spectroscopy of impurities in quantum gases*, Phys. Rev. A **102**, 023304 (2020).

[56] Y. Smirnov, *Talmi transformation for particles with different masses (II)*, Nucl. Phys. **39**, 346 (1962).

[57] J. Levinsen and S. K. Baur, *High-polarization limit of the quasi-two-dimensional Fermi gas*, Phys. Rev. A **86**, 041602(R) (2012).

[58] V. Pietilä, D. Pekker, Y. Nishida, and E. Demler, *Pairing instabilities in quasi-two-dimensional Fermi gases*, Phys. Rev. A **85**, 023621 (2012).